J Mater Sci (2011) 46:7169–7176
DOI 10.1007/s10853-011-5840-x

SIZE DEPENDENT EFFECTS

Crystallization of (Fe, Mn)-based nanoparticles in sodium-silicate glasses

Ruzha Harizanova · Ivailo Gugov · Christian Rüssel · Dragomir Tatchev · Vikram Singh Raghuwanshi · Armin Hoell

Received: 17 December 2010 / Accepted: 29 July 2011 / Published online: 6 August 2011

Abstract In this investigation, glasses from the system $Na_2O/MnO/SiO_2/Fe_2O_3$ are prepared using a conventional glass-melting technique. During annealing the glass, a nanocrystalline (Fe, Mn)-based spinel phase is precipitated. The phase composition and microstructure of the formed glass–ceramics are studied using X-ray diffraction and electron microscopy. Anomalous small-angle X-ray scattering experiment is used to gather information on the size, composition and element distribution for the precipitated (Fe, Mn)-based nanocrystals. The sizes of the formed spinel crystals, as determined by scanning electron microscopy and anomalous X-ray scattering, are in the range from 12 to 50 nm for annealing temperatures in the range from 550 to 700 °C. Annealing for a longer period of time at temperatures ≥600 °C results in the formation of a second crystalline phase, $NaFe(SiO_3)_2$ (aegirine). The ASAXS data show the formation of core–shell structure for the (Fe, Mn)-based crystals with core consisting mostly of iron oxide and a shell, depleted of Fe and Mn. The growth of the spinel crystals is assumed to be kinetically self-constrained.

R. Harizanova (✉) · I. Gugov
Department of Physics, University of Chemical Technology and Metallurgy, 1756 Sofia, Bulgaria
e-mail: ruza_harizanova@yahoo.com

C. Rüssel
Otto-Schott-Institut, Jena University, 07743 Jena, Germany

D. Tatchev
Institute of Physical Chemistry, Bulgarian Academy of Sciences, 1113 Sofia, Bulgaria

V. S. Raghuwanshi · A. Hoell
Institute of Applied Materials, Helmholtz Zentrum Berlin, 14109 Berlin, Germany

Introduction

In the past few decades, numerous reports on the synthesis and application of oxide glasses and glass–ceramics containing 3d-transition metal ions were published [1–20]. Oxide glasses with high concentrations of 3d-metals and glass–ceramics derived hereof containing magnetic nanocrystals are of both fundamental and practical interest due to their novel electrical and magnetic properties [21, 22]. The possibility to precipitate magnetic phases with crystallite sizes varying from some nanometres to some hundred nanometres enables a wide range of possible technical applications. They are, e.g. used as parts of cooling or shielding devices for various electronic components, as well as a component of ferrofluids used as solder materials [21]. Furthermore, they possess advantageous elastic properties if combined with appropriate polymer materials [22]. Depending on the phase composition, size and volume fraction of the magnetic particles, the precipitated crystals are used as parts of ferrofluids in magnetic resonance imaging and in biomagnetic sensors for the detection of different chemical and biochemical substances [23, 24].

The synthesis of nano-sized magnetic crystals is usually achieved by using wet chemical routes, i.e. by the precipitation of magnetite (Fe_3O_4) [25–28] but also of Co_3O_4 and $MnFe_2O_4$ [28, 29] from aqueous solutions. Furthermore, the synthesis of oxide glass–ceramics containing nano-sized ferrimagnetic or superparamagnetic particles is reported in the literature [16, 17]. The main problem associated with the synthesis of oxide glasses with high concentrations of transition metals using standard melting techniques is that the corresponding products may crystallize spontaneously [2, 3, 13, 30–34]. This may result in uncontrolled crystallite sizes and sometimes, phase composition [32–34]. The spontaneous crystallization during

cooling can be avoided or reduced by adjusting the glass composition (e.g. by decreasing the transition metal concentration) or by increasing the cooling rate [16, 17, 30]. Thermal annealing of the obtained glassy products enables the precipitation of crystalline phases with tailored size distribution of the particles [16, 17]. Furthermore, glassy or glass–ceramic materials containing large concentrations of transition metal oxides may be produced from natural minerals or wastes. Such glass–ceramics might be used as building materials, refractories and for the preparation of pigments [1, 2].

The effect of iron oxides, as well as the presence of a second transition metal oxide on the phase composition and microstructure has been reported [13, 31]. Whereas magnetite and hematite can easily be distinguished using X-ray diffraction (XRD), nanocrystals, e.g. of solid solutions containing two or more transition metals are difficult to characterize. In some cases, XRD does not allow the trustful separation of the main diffraction peaks of two nanocrystalline phases due to the relatively low intensity of the peaks and their significant broadness. The latter problem can be solved if advanced X-ray scattering techniques such as anomalous small-angle X-ray scattering (ASAXS) are used, [35–41]. ASAXS is an element-sensitive analysis technique, which allows to extract information about the dimensions of nanoparticles with sizes in the range from about 1 nm to some 100 nm. Simultaneously, the chemical composition of the crystals could be determined. This facilitates the phase recognition in complex multicomponent systems [35–38].

This article provides a study on the precipitation of nano-sized spinel phases from two glasses in the system $Na_2O/MnO/SiO_2/Fe_2O_3$ by using conventional glass-melting technique and subsequent thermal annealing. ASAXS enables to determine the size, the chemical composition and phase composition of the obtained nanocrystals.

Experimental procedure

The procedure used for the glass preparation and the used raw materials are the same as already described in Ref. [31]. Within the system $Na_2O/MnO/SiO_2/Fe_2O_3$ two glasses with the following compositions, given in mol%, were prepared:

- Glass A: $13.6Na_2O/8.5MnO/62.9SiO_2/15.0Fe_2O_{3-\delta}$ (reduction achieved by using $FeC_2O_4{\cdot}2H_2O$ as raw material).
- Glass B: $16Na_2O/10MnO/59SiO_2/15Fe_2O_3$ (Fe_2O_3 used as raw material).

The samples prepared using FeC_2O_4 as raw material are denoted in the following as 'reduced', while samples melted using Fe_2O_3 are designated as 'oxidized'. After pouring the melts into a pre-heated graphite mould, the resulting glasses were transferred to a muffle furnace and annealed at 480 °C for 10 min. Then the furnace was switched off and the glass was allowed to cool down with furnace velocity to room temperature.

In order to precipitate manganese and/or iron-containing crystals, glasses A and B were thermally annealed at temperatures in the range from 510 to 700 °C. The heating rate from room temperature to the desired annealing temperature was always 10 K/min. After annealing the samples for the desired time at the corresponding temperature, they are taken out of the furnace and let to cool down in air to room temperature. The annealing temperatures were clearly above the glass transition temperatures: $T_g = 490$ °C for glass A and $T_g = 494$ °C for glass B, [31]. Annealing times in the range from 10 min to 100 h were used.

The phase compositions were determined by XRD (Siemens, D 5000), using $Cu_{K\alpha}$-radiation; the 2θ-values were in the range from 10° to 60°. The microstructures were studied by scanning electron microscopy (SEM: JEOL 7001F), the samples were cut, polished and coated with carbon. Secondary (SE), as well as backscattered electrons were used for imaging.

Furthermore, information on the chemical and phase composition, as well as the average size of the precipitated nanocrystals was gathered by means of ASAXS. Small-angle X-ray scattering (SAXS) is a method widely used in the analysis of internal nanoscale structures [42] The technique provides a number of structural parameters such as sizes, volume fraction, or shape of particles, as well as their correlations in the case of a denser particle system. The scattering intensity from a dilute system of spherical particles embedded in a matrix and surrounded by a shell of different composition and/or density is described by

$$I(q,E) = N_p \int \left[F(q,R,\Delta\eta) - F(q,vR,\Delta\eta(1-\mu))\right]^2 N(R)\mathrm{d}R + B \quad (1)$$

where

$$F(q,R,\Delta\eta) = \frac{4}{3}\pi R^3 \Delta\eta \cdot 3 \cdot \frac{\sin(q\cdot R) - (q\cdot R)\cos(q\cdot R)}{(q\cdot R)^3}$$

is the normalized particle form factor, $\Delta\eta$ is the scattering contrast between the shell and the matrix, $\Delta\eta\mu$ the contrast core–matrix, R is the outer radius of the shell, and vR is the core radius, i.e. the inner radius of the shell. Here, q means the scattering vector length. Its magnitude is defined as $q = 4\pi\sin(\theta)/\lambda$, where θ is the half scattering angle and λ the wavelength. $N(R)$ denotes the particle size distribution, assumed to be lognormal, and N_p is the total number of

particles per unit volume. In addition to SAXS, ASAXS allows element specific contrast variation between different phases in the sample and hence the possibility to determine phase compositions [43–46]. The scattering contrasts $\Delta\eta$ and $\Delta\eta\mu$ depend monotonically on the X-ray energy. The contrast variation in ASAXS is due to energy dependency of the atomic scattering factor $f(E)$, in particular, in the vicinity of X-ray absorption edges. The atomic scattering factor $f(E)$ can be written as:

$$f(E) = f_0 + f'(E) + if''(E) \quad (2)$$

with the atomic form factor $f_0 = Z$ (atomic number) $f'(E)$ and $f''(E)$ being additional anomalous contributions. The factors $f'(E)$ and $f''(E)$ are connected to each other via Kramers–Kronig relations. Both factors can be calculated for free atoms using the method of Cromer and Liberman [47]. The effective electron densities ηp and ηm are linearly correlated with the atomic scattering factor $f(E)$ in Eq. 2. In this study, chemical compositions of the nanocrystals and the remaining glass matrix were determined by means of ASAXS. The ASAXS measurements were performed at 7T-MPW-SAXS beamline at Helmholtz Zentrum Berlin (BESSY II). The study was performed in transmission geometry. The sample thicknesses were between 100 and 200 μm. Five or six X-ray energies close, but below the K-absorption edges of Fe and Mn, 7112 and 6539 eV, respectively, were used. The data were recorded with a position sensitive multi-wire proportional counter gas detector. A gassy carbon was used as a secondary standard for calibrating of the scattered intensity into absolute scattering units. Corrections for the detector sensitivity, scattering background, detector dead time, solid angle correction, primary beam intensity, and absorption normalization were done with a beamline dedicated software.

Results

The oxidized glass B with composition $16Na_2O/10MnO/59SiO_2/15Fe_2O_3$ and the reduced glass A with the composition $13.6Na_2O/8.5MnO/62.9SiO_2/15.0Fe_2O_{3-\delta}$ showed the formation of a nanocrystalline spinel phase, after annealing at temperatures above T_g. Figures 1 and 2 show that after annealing at temperatures up to 600 °C, the formation of $(Mn_{0.6}, Fe_{0.4})(Mn_{0.4},Fe_{1.6})O_4$ (JCPDS 88-1965) or Fe_3O_4 (JCPDS 87-2334) is observed for both samples A and B. Actually, the precipitated phase may be described as a solid solution of a mixed spinel type $(Fe^{2+}, Mn^{2+})(Fe^{3+}, Mn^{3+})_2O_4$. However, with respect to the relatively broad peaks and the proximity of the main reflexes of the two phases (the difference in the main peak positions is $\sim 0.7°$), an exact determination of the chemical composition of the formed crystalline phase only by means of XRD was

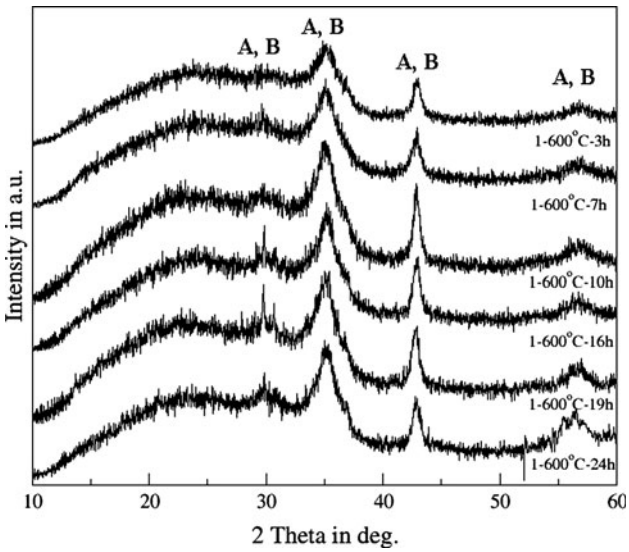

Fig. 1 XRD patterns of samples from the composition A ($13.6Na_2O/8.5MnO/62.9SiO_2/15.0Fe_2O_{3-\delta}$), annealed at 600 °C for different times (formation of mixed crystals $MnFe_2O_4$ (*A*) and Fe_3O_4 (*B*))

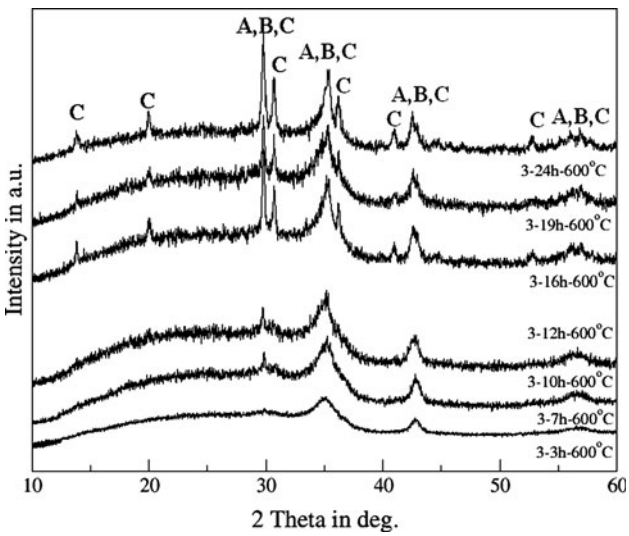

Fig. 2 XRD patterns of samples from the composition B, annealed at 600 °C for different times—formation of mixed crystals $MnFe_2O_4$ (*A*) and Fe_3O_4 (*B*), as well as of $NaFe(SiO_3)_2$ (*C*)

impossible. As seen in Fig. 2, for the sample B also a second crystalline phase, aegirine, $NaFe(SiO_3)_2$ (JCPDS 34-185) is detected by the XRD.

In the microstructure of the sample A annealed at a temperature of 550 °C, only one morphological type of crystals is observed by SEM for all supplied annealing times (see Fig. 3a, b). The formed phase, according to the XRD patterns, is the spinel phase $(Fe^{2+}, Mn^{2+})(Fe^{3+}, Mn^{3+})_2O_4$. The image analysis of Fig. 3a revealed a relatively broad size distribution of particles, centred at about 50 ± 1 nm. Two types of crystals are formed after

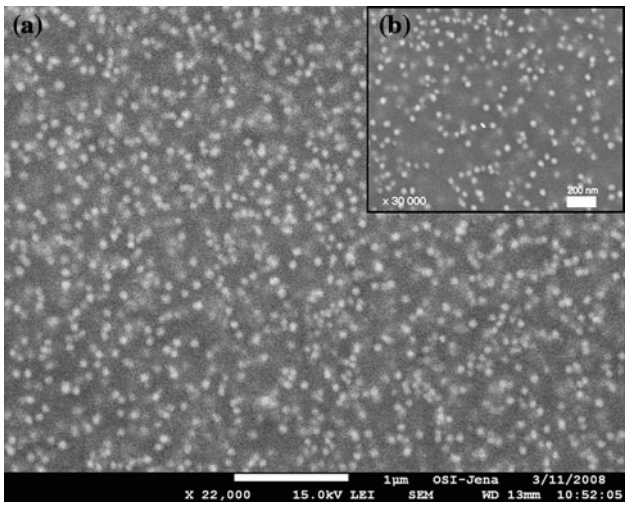

Fig. 3 **a** SEM (SE) image of C-covered sample from composition A, annealed for 3 h at 550 °C—uniform distribution of the (Fe, Mn)-based crystals, which are the only crystalline phase present. **b** SEM (SE) image of C-covered sample from composition A, annealed for 3 h at 550 °C—higher magnification of the nearly round-shaped nanocrystals

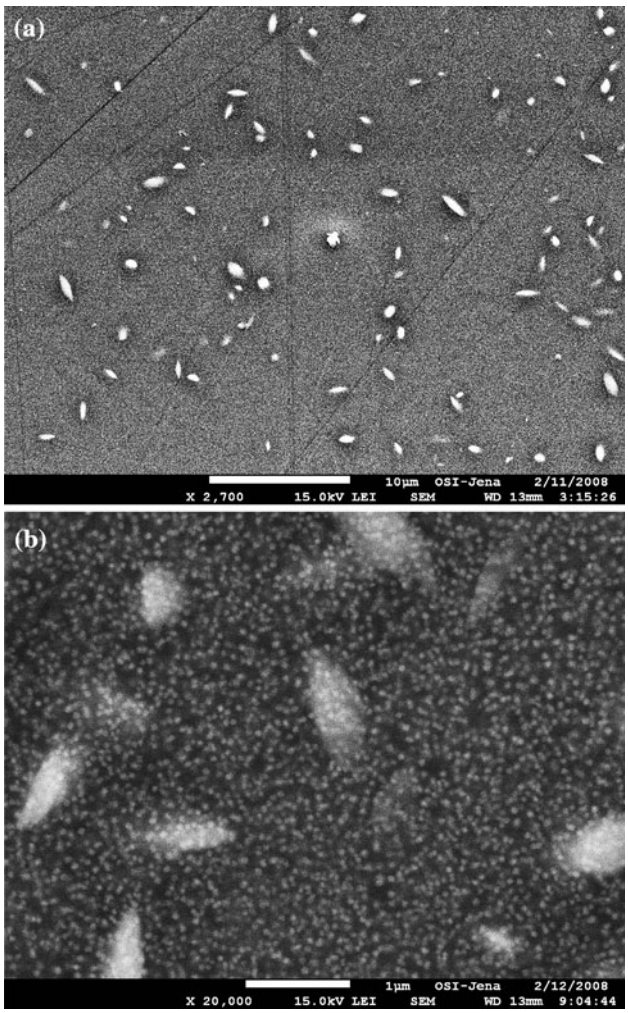

Fig. 4 **a** SEM (SE) image of C-covered sample from composition A, annealed for 16 h at 600 °C—uniform distribution of the nano-sized (Fe, Mn)-based crystals and formation of a second crystalline phase which corresponds to the large ellipsoidal crystals. **b** SEM (SE) image of C-covered sample from composition A, crystallized for 16 h at 600 °C—higher magnification of the two types of crystalline phases formed, showing their morphological differences

annealing of glass A for 16 h at 600 °C. The SEM micrographs of this sample are shown in Fig. 4a and b. The population of small crystals with mean size of about 50 ± 1 nm is similar to those in Fig. 3a and b. Here, however, large elongated crystals with sizes up to 1,000 nm are formed too. The volume fraction of this phase is relatively low and, hence, the reflexes at the XRD patterns of the precipitated $NaFe(SiO_3)_2$ phase are not so pronounced as in the case of annealed samples B (cf. Figs. 1, 2).

The crystallization of glass B follows a similar scenario. The comparison of Figs. 1 and 2 as well as of Figs. 4 and 5 shows that, however, a larger volume fraction of aegirine is formed here for shorter annealing times and at lower annealing temperatures.

It should be noted that aegirine is neither ferro- nor ferrimagnetic. Figure 6a shows that a further increase in the annealing temperature or time for the samples with composition B leads to formation of $NaFe(SiO_3)_2$ crystals with predominantly ellipsoidal shape and sizes in the range from 5 to 20 ± 0.1 µm. In between the large crystals still tiny spherical crystals, corresponding to the spinel phase, are observed—as seen in Fig. 6b.

Due to the difficulties in the phase identification using conventional XRD, we also applied ASAXS technique to samples A, annealed at 550 °C for different periods of time. This was done, to get additional information on the phase composition, the volume fraction and the size distribution of the particles. Conventional XRD simply reveals the formation of Fe- or Fe and Mn-based spinel phases during the thermal annealing of the glasses. Using normal SAXS, the scattering factor is independent of the photon energy and equal to the atomic number Z. By contrast, for ASAXS, the energy dependent scattering factors play an important part. Each element has its own characteristic absorption edge, and hence, the variation of the photon energy near the absorption edge provides a selective way to change the contribution of a particular chemical element to the total intensity scattered by the samples. The atomic scattering factors are known and tabulated in a number of available sources. The variation of the second power of the real part of the complex atomic scattering factors of Fe and Mn are shown in Fig. 7. The symbols mark the X-ray energies at which measurement was performed.

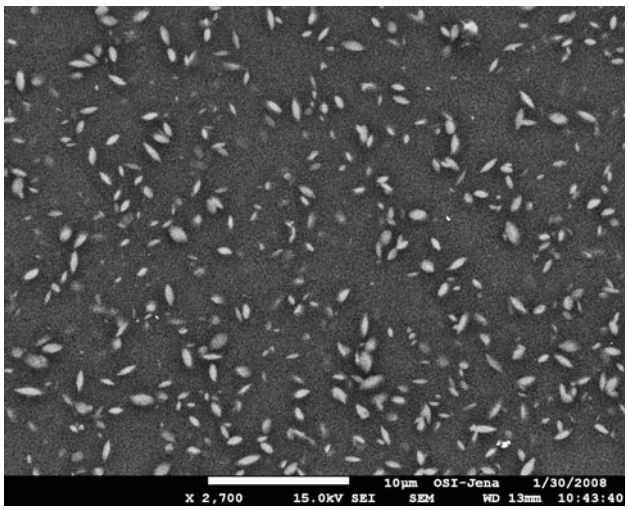

Fig. 5 SEM (SE) image of C-covered sample B, crystallized for 10 h at 600 °C—uniform distribution of the nano-sized (Fe, Mn)-based crystals and clearly pronounced formation of a second crystalline phase, obviously corresponding to the $NaFe(SiO_3)_2$

We performed the ASAXS experiments on several annealed glass samples at the Fe and Mn K-edges. Figure 8 shows typical ASAXS effect at the Fe K-absorption edge of a sample of type A annealed at 550 °C for 60 min. The analysis shows that while approaching the absorption edge, the scattering intensity decreases because the real part of the atomic scattering factor belonging to Fe atoms decreases as depicted in Fig. 7. The same experiment was performed at the Mn-edge and shows similar, but much smaller ASAXS effect. The presented curves provide information on the particle size, distribution and the content of the resonant element in the particle, as already observed for other multicomponent systems [37, 38]. The experimental data were analysed by applying the models of homogeneous sphere and spherical core–shell particle by assuming lognormal size distribution. The homogeneous sphere model was unable to fit the scattering curves. Thus, the core–shell model, which represents inhomogeneous, but spherically symmetrical particles, was applied. Such particle may consist of two different phases one representing the core, and another representing the shell or a single phase particle which composition and/or density varies along its radius. The spherical shape is proved by the SEM observations—Fig. 3a and b. The current data processing shows particle average core radius between 5 and 23 nm and mean shell thickness around 1–2 nm, as well as average particle size, for samples annealed at 550 °C for periods between 40 and 180 min—data given in Table 1.

In case of ASAXS the squared scattering contrasts, i.e. the second power of the effective electron density difference between two phases is a fit parameter while fitting simultaneously a set of all scattering curves of a sample

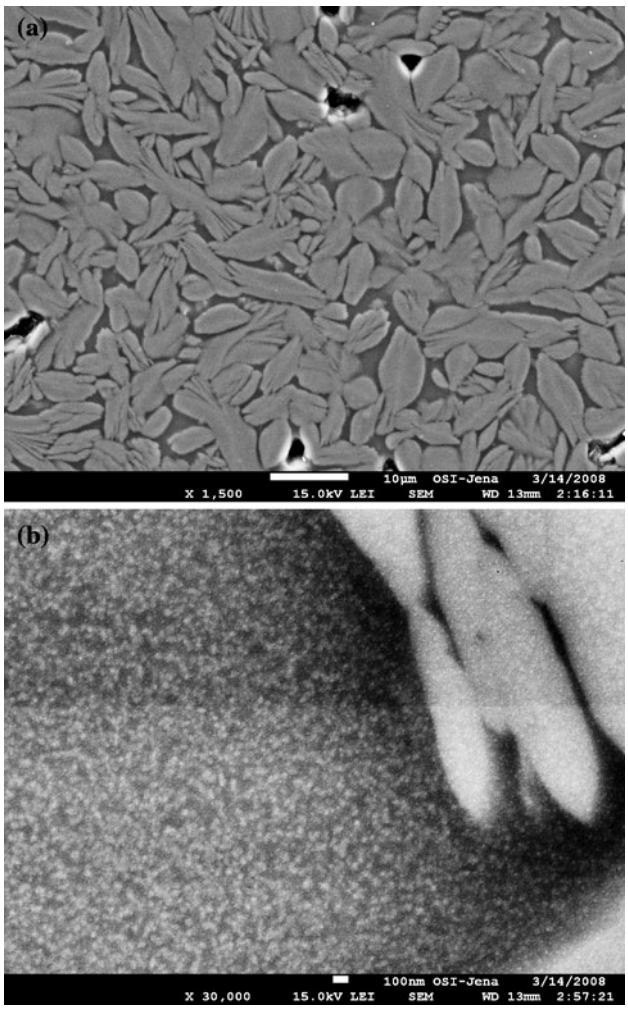

Fig. 6 **a** SEM (SE) image of C-covered sample B, crystallized for 24 h at 650 °C—prevailing formation of large ellipsoidal shaped $NaFe(SiO_3)_2$ crystals. **b** SEM (SE) image of C-covered sample B, crystallized for 24 h at 650 °C—formation of nano-sized crystals between the large ellipsoidal shaped $NaFe(SiO_3)_2$ crystals

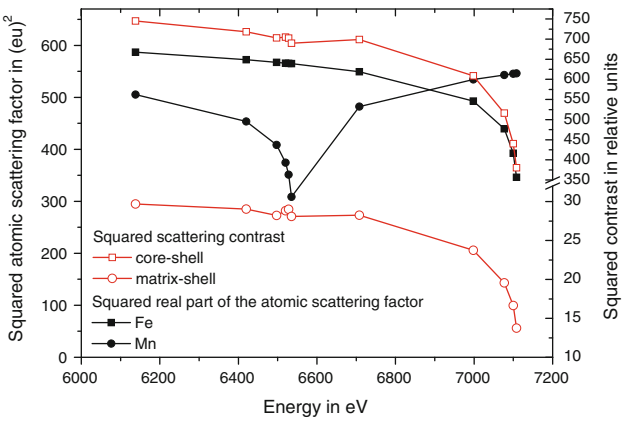

Fig. 7 The squared scattering contrast determined by fitting of 11 scattering curves of a sample of type A annealed for 1 h at 550 °C compared with the squared real part of the atomic scattering factors of Fe and Mn

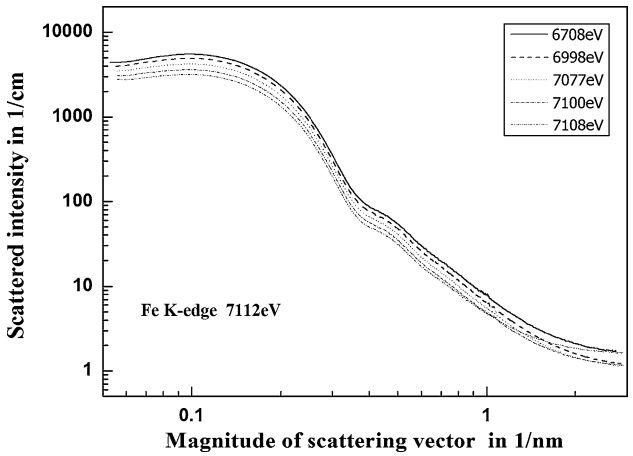

Fig. 8 ASAXS close to the Fe–K absorption edge (7112 eV) of a sample of type A annealed for 1 h at 550 °C

measured near both absorption edges. The squared scattering contrasts for a sample annealed for 1 h at 550 °C are also shown in Fig. 7. Since the magnitude of the anomalous scattering effect depends on the difference of both the content of the resonant elements (Fe and Mn) and the mass density difference between the pairs of phases (core–shell and matrix–shell), the composition of the phases can be assessed only qualitatively. Thus, from Fig. 7 and from the fit model we conclude that the shell contains less Fe than the matrix and the core, while the core contains more Fe. The same applies also for Mn, but the difference is much smaller. Keeping in mind that the amount of Mn is only half as large as the content of Fe in the glass and that the depth of the Mn absorption edge (Fig. 7) is nearly the same as that of Fe one may conclude that Mn is more homogeneously distributed between the three phases, particle core, shell and glass matrix. The content of Fe in the particle core is much larger than that of Mn. Thus, according to the ASAXS results, the particles have compositions close to Fe_3O_4 with only small amount of Mn atoms replacing the Fe atoms. A shell devoid of Fe and probably Mn is formed around the particle. The results suggest that the mass density of the shell only slightly differs from the density of the glass matrix. Thus, the shell is actually a depleted of Fe diffusion zone. A nonmagnetic shell around magnetic magnetite particles in glass was described earlier by combining X-ray and neutron small-angle scattering [48].

The volume fraction of the particles is a variable coupled with the particle composition and cannot be determined without thorough quantitative analysis. From the decrease of the scattered intensity at very small angles, as in Fig. 8, one may conclude that the volume fraction is over 6–7%. Only for the sample annealed for shortest time—20 min at 550 °C—such intensity decrease at smallest angles is not present.

Discussion

The glass formation for the oxidized sample B and the reduced sample A might be explained with the different incorporations of the Fe^{2+} and Fe^{3+} ions in the glass network as observed in the case of iron oxide concentrations up to 2 mol%, [49–55] and is already discussed in [31]. As described in [31], the oxidized sample with the composition of sample A already contains some quantity of nanocrystals. The ability to form glasses might also be affected by the redox ratio Fe^{2+}/Fe^{3+} which is supposed to be different in the oxidized and reduced samples. The sample A is attributed to a higher acidity of the glass matrix, i.e. here the SiO_2-concentration is higher and the alkali concentration is lower, according to the acidity–basicity concept, as suggested by Duffy, [51] and Duffy and Ingram, [56]. At the same time, the sample B has higher alkali concentration and lower SiO_2 content, i.e. this sample is with higher basicity. The latter determines the higher concentration of the ferric ions in comparison to the

Table 1 Phase formation and crystal size in the samples A and B, according to the applied time–temperature annealing programs

Time–temperature program		Sample A Phases formed and crystal size	Sample B Phases formed and crystal size
550 °C	40 min	Spinel—SAXS: 14 ± 0.5 nm	
	1 h	Spinel—SAXS: 24 ± 0.5 nm	–
	3 h	Spinel—SEM: 50 ± 1 nm; SAXS: 44±0.5 nm	–
	7 h	–	–
550 °C	10–24 h	Spinel—SEM: 50 ± 1 nm	Spinel
600 °C	3–7 h	Spinel	Spinel, aegirine (SEM data)
		Spinel—SEM: 40 ± 1 nm	
600 °C	10–24 h	Spinel—SEM: 40 ± 1 nm, aegirine (SEM data)	Aegirine, spinel (SEM, XRD data)
650 °C	3–24 h	Spinel, aegirine (SEM, XRD data)	Spinel, aegirine (SEM, XRD data)
700 °C	3–24 h	Spinel, aegirine (SEM, XRD data)	–

concentration of the ferrous ones [51]. The iron ions, depending on both their oxidation state and concentration, can be incorporated in the silicate glass matrix either in tetrahedral or in octahedral coordination. In the case Fe^{3+} is incorporated in the glass matrix in tetrahedral coordination, i.e. as FeO_4^-, the formally negative charge must be compensated preferably by Na^+-ions. With decreasing concentration of Na^+, the stabilisation of FeO_4^--tetrahedra decreases and as a result, the formation of iron-rich clusters occurs [57]. Due to the higher acidity, the number of Na^+-ions which may compensate the charge of FeO_4^--tetrahedra is smaller in the sample A. Thus, the number of sites for the Fe^{3+}-ions which can be incorporated homogeneously in the glass network is smaller and the tendency for clustering increases. Clustering has also been described for silicate glasses solely doped with Fe-ions [49–53, 55]. As a result, in the sample with the composition $13.6Na_2O/8.5MnO/62.9SiO_2/15.0Fe_2O_3$, the formation of nano-sized crystals during cooling of the melt is observed [31], while the sample B with the same Fe_2O_3-concentration and cooled applying the same parameters is still amorphous. It is known, that at high temperatures, Fe^{2+}, Fe^{3+} and the physically dissolved oxygen are in equilibrium, [52, 53] and the equilibrium is shifted to the reduced state, with increasing temperature, as described for similar iron-containing silicate systems [52–54, 57–59]—the same we expect in our system. Additionally, we established in our investigation, that as already observed for other compositions from the system $Na_2O/MnO/SiO_2/Fe_2O_3$, [31] the raw materials, i.e. oxidizing or reducing components of the batch are decisive and the furnace atmosphere has only a minor effect on the Fe^{2+}/Fe^{3+}-ratio. The latter is also seen from data in Table 1 for the crystallization behaviour of samples A and B, where the aegirine phase appears at lower annealing times in sample B compared to sample A. However, despite the high melting temperature, the concentration of ferric ions (Fe^{3+}) is considerable—as suggested in literature for smaller iron oxide concentrations, [49, 50, 53–55] and hence, the formation of the NaFe$(SiO_3)_2$ phase becomes possible. As shown in [57] at an oxygen activity of the melt in the range from 0.21 (air) to 1 bar (oxygen), only 10–25% of the total iron occurs as Fe^{2+} at the maximum melting temperature supplied (1400–1500 °C). An oxygen activity of 1 bar means that the melt is in equilibrium with an atmosphere of 1 bar oxygen. For the formation of $MnFe_2O_4$ or rather a mixed spinel phase of the type (Fe^{2+}, Mn^{2+}) (Fe^{3+}, Mn^{3+})$_2O_4$ (as also suggested in Ref. [25]), the valence state in which manganese occurs in the glass is very important. Also in the case of manganese containing glasses, a similar redox equilibrium to that described above for Fe is also formed. In contrast to the Fe^{2+}/Fe^{3+}-equilibrium, the oxidized species, Mn^{3+} occurs only in minor quantities ($[Mn^{2+}]/[Mn^{3+}] > 20$) as, e.g. reported by Gravanis et. al. [54, 58, 59]. Thus, the addition of both manganese and iron oxide enables the crystallization of a solid solution of the spinel (Fe, Mn)$_3O_4$ phase or more precisely, of a phase from the type (Fe^{2+}, Mn^{2+}) (Fe^{3+}, Mn^{3+})$_2O_4$, in which the corresponding quantities of di- and trivalent ions are incorporated. The addition of reducing agents, i.e. FeC_2O_4 does not change the type of the crystallizing spinel species, as shown in Figs. 1, 2, 3, 4, 5, 6 and in Table 1. This addition, however, affects the crystallization of the NaFe$(SiO_3)_2$ (aegirine) phase.

For the crystallized samples with the composition B, the formation of aegirine is observed in larger amounts and for smaller annealing times in comparison to the samples with the composition A, see Table 1. The latter can be explained by the higher concentration of Fe^{3+}-ions in the case of B. Actually, as shown in the SEM-micrograph in Fig. 5, in the sample B, annealed for 10 h at 600 °C, nano-sized crystals of the iron-manganese spinel and additionally crystals of ellipsoidal shape are present in notable quantities. The ellipsoidal phase, according to the XRD data, should be attributed to aegirine. In the annealed samples A, where the SiO_2 concentration and Fe^{2+}/Fe^{3+}-ratio is larger, the crystallization of NaFe$(SiO_3)_2$ is suppressed for temperatures up to 600 °C and annealing times up to 16 h (see Figs. 3a, b, 4a, b; Table 1).

The sizes of the spinel nanocrystals, determined from the XRD line broadening for the set of samples A range from 12 to 17 ± 1 nm which is much smaller than the sizes of 50 ± 1 nm found by SEM and ASAXS for samples annealed for 3 h at 550 °C. The line broadening in these samples mainly results from the overlapping of the reflexes of the two spinel phases: ($Mn_{0.6}$, $Fe_{0.4}$) ($Mn_{0.4}$,$Fe_{1.6}$)O_4 and Fe_3O_4. The particle sizes as determined from the SEM images, as well as from the ASAXS, are in the range from 12 to 50 nm and do not change if the annealing time is longer than 3 h. It is observed that only the volume fraction of the nano-sized crystalline phase increases while increasing the annealing temperature. This type of crystallization kinetics suggests the idea that the growth of the spinel phase in the samples A is kinetically self-constrained, as already observed for other, non-iron containing, glass–ceramics [17, 60–62]. As seen from the ASAXS data, the concentration of iron and manganese ions decreases in vicinity of the growing spinel crystal. This information, allows to assume that around the crystals a silica-rich shell with rapidly increasing viscosity is formed. Further, it is expected: if the glass transition temperature of this shell approaches the annealing temperature, the crystal growth is decelerated and finally stops for kinetic reasons. As it is seen in Figs. 4a and b; 5 and 6a and b the silica

containing aegirine phase has much smaller nucleation rate and much higher crystal growth velocity in comparison to those of the spinel phase.

The formation of core–shell crystals revealed from the ASAXS studies could be explained as follows: an iron enriched core spinel phase nucleates homogeneously and starts growing. At some point, the rising concentration of manganese in the surrounding melt causes heterogeneous nucleation and growth of manganese enriched spinel phase. The heterogeneous nucleation and the subsequent epitaxial growth are facilitated by the proximity between the lattice constants of both spinel phases. A viscous shell, depleted in both iron and manganese is formed around the growing crystal.

Conclusion

Crystalline spinel of the type $(Mn^{2+}, Fe^{2+})(Fe^{3+},Mn^{3+})_2O_4$ is precipitated in the two investigated compositions with 15 mol% Fe-oxide for temperatures up to 600 °C, while at 600 °C for longer annealing times also a second crystalline phase—aegirine, $NaFe(SiO_3)_2$—is formed. The precipitation of hematite is avoided in the whole temperature interval investigated for both reduced and oxidized compositions. For crystallization times > 3 h and temperatures lower than 600 °C, the size of the formed nanocrystals hardly changes with time and varies from 12 to 50 nm. The elemental composition and the size of the obtained nanoparticles, as studied by ASAXS for the sample annealed for 60 min at 550 °C, show formation of Fe-rich nanocrystals containing small amount of Mn with radii varying from 6 to 25 nm and surrounded by shell devoid of both Fe and Mn. Kinetically self-constrained growth mechanism of the spinel crystals is assumed in the obtained glass–ceramic materials.

Acknowledgements This study was partially supported by contract 10-760/2010 of the University of Chemical Technology and Metallurgy. Further, we acknowledge the Helmholtz Zentrum Berlin—Electron storage ring BESSY II—for provision of synchrotron radiation at 7T-MPW-SAXS beamline. The research leading to these results has received funding from the European Community's Seventh Framework Programme (FP7/2007-2013) under grant agreement No. 226716.

References

1. Karamanov A, Pelino M (2001) J Non-Cryst Solids 281:139
2. Romero M, Rincon JM (1999) J Am Ceram Soc 82:1313
3. Ehrt D, Reiß H, Vogel W (1976) Silikattechnik 27:304
4. Adler D (1985) J Non-Cryst Solids 73:205
5. Owen AE, Spear WE (1976) Phys Chem Glasses 17:174
6. Mott NF (1968) J Non-Cryst Solids 1:1
7. Mackenzie JD (1970) J Non-Cryst Solids 2:16
8. Klinger MI (1968) Rep Prog Phys 31:225
9. Schmidt AP (1970) J Appl Phys 39:3140
10. Murawski L, Chung CH, Mackenzie JD (1979) J Non-Cryst Solids 32:91
11. Mackenzie JD (1964) J Am Ceram Soc 47:211
12. Mackenzie JD (1964) In: Mackenzie JD (ed) Modern aspects of the vitreous state, vol 3, Butterworths, London
13. Trap HJL, Stevels JM (1963) Phys Chem Glasses 4:193
14. Anderson RA, MacCrone RK (1974) J Non-Cryst Solids 14:112
15. Allersma J, Mackenzie JD (1967) J Chem Phys 47:1406
16. Woltz S, Hiergeist R, Görnert P, Rüssel C (2006) J Magn Magn Mater 298:7
17. Woltz S, Rüssel C (2004) J Non-Cryst Solids 337:226
18. Qiu HH, Kudo M, Sakata H (1997) Mater Chem Phys 51:233
19. Qiu HH, Mori H, Sakata H, Hirayama T (1995) J Ceram Soc Jpn 103:32
20. Roy S, Chakravorty D (1994) J Mater Res 9:2314
21. Odenbach S (2004) J Phys 16:1135
22. Zhou GY et al (2004) Smart Mater Struct 13:309
23. Sakai Y et al (1995) J Ferment Bioeng 80:300
24. Aytur T et al (2006) J Immunol Methods 314:21
25. Zhang ZJ et al (1998) J Am Chem Soc 120:1800
26. Wang X, Li Y (2007) Chem Commun. 2901–2910. doi:10.1039/b700183e
27. Si H et al (2008) J Colloid Interface Sci 327:466
28. Shi W, Chopra N (2010) J Nanopart Res. doi:10.1007/s11051-010-0086-0
29. Herranz T et al (2006) Chem Mater 18:2364
30. Harizanova R, Völksch G, Rüssel C (2010) J Mater Sci 45:1350. doi:10.1007/s10853-009-4090-7
31. Harizanova R, Völksch G, Rüssel C (2010) Mater Res Bull 46: 81–86. doi:10.1016/j.materresbull.2010.09.036
32. Völksch G et al (2004) Glastech Ber Glass Sci Technol 77C:438
33. Harizanova R, Keding R, Rüssel C (2008) J Non-Cryst Solids 354:65
34. Harizanova R et al (2008) Eur J Glass Sci Technol B 49:177
35. Hoell A et al. German patent: DE 10 2006 029 449
36. Tatchev D (2008) Phil Mag 88:1751
37. Haas S et al (2010) Phys Rev B 81: 184207
38. Tatchev D (2010) J Appl Cryst 43:8
39. Simon J-P (2007) J Appl Crystallogr 40: S1
40. Lembke U et al (1997) J Appl Crystallogr 30:1056
41. Lembke U, Kranold R (1995) Nucl Instrum Methods Phys Res B 97:190
42. Guinier A, Fournet G (1955) Small-angle scattering of X-rays. Wiley, New York
43. Goerigk G et al (2003) J Appl Crystallogr 36:425
44. Hoell A et al (2001) Scr Mater 44:2335
45. Haas S et al (2008) ECS Trans 6:127
46. Zehl G et al (2007) Angew Chem Int Ed 46:7311
47. Cromer D, Liebermann D (1970) J Chem Phys 53:1891
48. Lembke U et al (1999) J Appl Phys 85:2279
49. Rüssel C, Wiedenroth A (2004) Chem Geol 213:125
50. Levy RA, Lupis CH, Flinn PA (1976) Phys Chem Glasses 17:94
51. Duffy A (1999) Phys Chem Glasses 40:54
52. Wiedenroth A, Rüssel C (2004) J Non-Cryst Solids 347:180
53. Wiedenroth A, Rüssel C (2002) J Non-Cryst Solids 297:173
54. Gravanis G, Rüssel C (1989) Glastech Ber 62:345
55. Bingham PA et al (1999) J Non-Cryst Solids 253:203
56. Duffy JA, Ingram MD (1976) J Non-Cryst Solids 21:373
57. Pye LD, Montenero A, Joseph I (eds) (2005) Properties of glass-forming melts. Taylor & Francis, Boca Raton
58. Kido L, Müller M, Rüssel C (2005) Chem Mater 17:3929
59. Kido L, Müller M, Rüssel C (2005) J Non-Cryst Solids 351:523
60. Rüssel C (2005) Chem Mater 17:5843
61. Bocker C, Rüssel C (2009) J Eur Ceram Soc 29:1221
62. Bhattacharya S, Bocker C, Heil T, Jinschek JR, Höche T, Rüssel C, Kohl H (2009) Nano Lett 9:2493